

This is the accepted manuscript made available via CHORUS. The article has been published as:

Wet-Chemical Synthesis of Enhanced-Thermopower $\text{Bi}_{1-x}\text{Sb}_x$ Nanowire Composites for Solid-State Active Cooling of Electronics

K. Vandaele, Bin He, P. Van Der Voort, K. De Buysse, and J. P. Heremans

Phys. Rev. Applied **9**, 024020 — Published 20 February 2018

DOI: [10.1103/PhysRevApplied.9.024020](https://doi.org/10.1103/PhysRevApplied.9.024020)

1 **Wet-chemical synthesis of enhanced-thermopower $\text{Bi}_{1-x}\text{Sb}_x$ nanowire composites for solid-**
2 **state active cooling of electronics**
3

4 K. Vandaele^{1,2}, Bin He¹, P. Van Der Voort², K. De Buysser² and J. P. Heremans^{1,3,4}

5 ¹Department of Mechanical and Aerospace Engineering, Columbus, Ohio, 43210, USA

6 ²Department of Inorganic and Physical Chemistry, Ghent University, Krijgslaan
7 281 - S3, 9000 Gent, Belgium.

8 ³Department of Physics, The Ohio State University, Columbus, Ohio, 43210, USA

9 ⁴Department of Materials Science and Engineering, The Ohio State University, Columbus, Ohio,
10 43210, USA

11
12 PACS: 72.15.Jf, 72.20.Pa, 72.10.-d

13
14 **Abstract**
15

16 In 1993, Hicks and Dresselhaus suggested that Bi nanowires could result in values of the
17 thermoelectric figure of merit $zT > 1$. The Dresselhaus group also calculated a ternary phase
18 diagram for $\text{Bi}_{1-x}\text{Sb}_x$ nanowires as a function of x and wire diameter. This manuscript reports a
19 new, wet-chemical method to synthesize $\text{Bi}_{1-x}\text{Sb}_x$ /silica nanowire composites. Resistivity, Hall
20 electron concentration, electron mobility, Seebeck and Nernst coefficients, and thermal
21 conductivity of composites were measured and compared to bulk polycrystalline $\text{Bi}_{1-x}\text{Sb}_x$
22 samples prepared either by ingot casting or by the same wet chemistry, but without
23 nanostructuring. A clear increase of the thermopower in 20 nm $\text{Bi}_{94}\text{Sb}_6$ /silica is reported when
24 compared to bulk samples, and the values are the highest found in the literature from 300 to 380
25 K, even though the electron concentration is higher than in the bulk. This suggests that,
26 consistent with theory, size quantization is responsible for the thermopower increase.
27

1. Introduction

Peltier-effect based solid-state cooling possesses many advantages over conventional cooling provided by thermodynamic cycles namely vibration-free operation from the absence of moving parts, a long lifetime, reliability, and compactness. Further, if we consider an ideal heat exchanger, thermoelectric (TE) devices have an extremely high specific cooling capacity. TE devices also have a short thermal response time. Their efficiency (today equivalent to 25% of that of vapor-compression coolers) is determined by the TE figure of merit of the materials, zT , which depends on thermal conductivity κ , electrical conductivity σ , and Seebeck coefficient α . Note that zT refers to the materials' figure of merit, whereas ZT is the device's figure merit (contribution of n-type and p-type legs). Together with the absolute temperatures of the hot side and the cold side of a thermoelectric energy converter (which determine its Carnot efficiency), the figure of merit zT of the thermoelectric materials governs its thermal efficiency. Here $zT \equiv \alpha^2 \sigma T / \kappa$, where α is the thermopower of the material, κ and σ are its thermal and electrical conductivities respectively, and T is the average temperature. By separating the electronic (κ_E) and lattice (κ_L) thermal conductivities, and applying the Wiedemann-Franz-Lorenz law ($\kappa_E = LT\sigma$, where $L \approx 1.6$ to $2.5 \times 10^{-8} \text{V}^2/\text{K}^2$ is the Lorenz ratio), the figure of merit becomes $zT = \alpha^2 / L \left(1 + \kappa_L / \kappa_E \right)^{-1}$. This illustrates how important it is to maximize α , and how only κ_L should be minimized, whereas a high κ_E is actually beneficial to zT .

The vast majority of applications for TE technology are in cooling applications such as automotive climate control via cooled seats, medical and scientific instrumentation, and camping gear. A large expansion of these applications into active TE cooling for thermal management of electronic circuits and batteries might be possible if the zT were enhanced enough and the

materials cost sufficiently controlled. Choosing between active TE cooling and passive cooling of such devices depends on the ratio between the required device temperature T_d and the temperature T_a at which the heat can be rejected. Active TE cooling implies that the heat exchanger system not only must handle the heat load from the device, but also that generated by the TE device itself, which is related to the TE figure of merit of the device (ZT). In the supplement¹, we show how this consideration imposes the condition

$$T_d < T_a \frac{1 + \sqrt{1 + ZT}}{2} \quad (1).$$

Only if condition (1) is met will an active TE cooler be more compact than a passive cooler. Given the importance of heat management to developing batteries and electronic circuits, zT improvements for cooling materials could have great technological impact. Cryogenic coolers are another potential field of applications. Today's six-stage Peltier coolers can reach temperatures as low as 170 K for a hot side of 300 K. Enhancements in the material's zT below room temperature could impact the cooling of IR detectors and other sensors in which thermal noise must be minimized by keeping them at temperatures below ambient.

Unfortunately, the interdependence of the material properties determining zT and their counter-indicated nature makes it difficult to increase zT . By far, the best cooling materials near room temperature are tetradymites, generally $(\text{Bi}_{1-x}\text{Sb}_x)_2(\text{Te}_{1-y}\text{Se}_y)_3$ compound semiconductors that crystallize with the $\bar{3}m$ space group. This is because the strong spin-orbit coupling in those compounds results in a very high electron mobility, while the high degeneracy of the pockets that form the Fermi surface result in a favorable thermopower.² The same arguments hold for $\text{Bi}_{1-x}\text{Sb}_x$ alloys. These are particularly suitable below room temperature. Until now, they have not been considered seriously for applications because, in bulk, they must be used as mechanically fragile single crystals. Preparing bulk $\text{Bi}_{1-x}\text{Sb}_x$ TEs is also difficult because the large temperature

1 difference between the liquidus and solidus impedes the reasonably accurate control of x .³ The
2 wet-chemistry route described here circumvents this problem.

3 Hicks and Dresselhaus predicted that zT would be enhanced greatly in quantum well⁴ and
4 wire⁵ structures because size-quantization effects result in a sharpening of the features of the
5 density of states (DOS), in turn, increasing the thermopower. Due to its charge carriers' small
6 effective mass, particularly electrons,^{6,7,8} elemental Bi was the chosen paradigm for this effect.

7 Bulk Bi is a semimetal⁹ with valence bands (VB) centered around the Brillouin zone (BZ)
8 T-points; the Fermi level cuts these VBs about 11 meV below their extremum. Conduction bands
9 are centered at the BZ L-points with L_s symmetry, which cut the Fermi energy ~ 27 meV above
10 their minimum, leading to an energy overlap of $E_{gTLs} = -38$ meV (a positive value indicates a
11 band gap; an energy overlap is treated as a negative band gap).⁹ Also at the L-point, there is a
12 VB of L_a symmetry, separated from the L_s band by a direct energy gap $E_{gLsa} = 13.6$ meV.⁶ In
13 semimetals, the electron and hole partial thermopowers counter each other; thus, the overall
14 thermopower is smaller than that of each separate carrier type, greatly reducing zT . Indeed, it was
15 predicted that if we could lift the band overlap in bulk Bi and reduce the electron density at room
16 temperature from the semimetal's $3 \times 10^{18} \text{ cm}^{-3}$ to $1 \times 10^{18} \text{ cm}^{-3}$ in this hypothetical semiconductor,
17 its zT could reach 1.3.¹⁰ Then, simply opening a gap by size quantization in the Bi electron band
18 structure should result in a great zT improvement. A theoretical calculation¹¹ predicted that zT
19 values >5 could be reached in 5 nm-diameter Bi nanowires via three effects: sharp features in the
20 DOS energy dependence, opening a gap, and reducing lattice thermal conductivity. This
21 promising result stimulated renewed TE research efforts.¹²

22 Early experiments on Bi nanowires and nanowire composites proved the theory
23 essentially correct. Two methods were developed to synthesize Bi nanowires inside porous

media, typically silica or alumina: high-pressure injection¹³ and in-situ vapor growth.¹⁴ It was shown experimentally¹⁵ that confining Bi into nanowires resulted in the opening of a band gap, as predicted¹¹ for wire diameters of 49 nm and below, although the mobility was reduced.¹⁶ The thermopower enhancement was observed experimentally in nanocomposites containing Bi nanowires with diameters decreasing from 50 to 9 nm.^{17,18}

Still, zT enhancement proved elusive. Thermal conduction through the porous matrix constitutes a thermal short,¹⁹ limiting the composite's effective zT . Because Bi oxidizes readily, sintered felts of nanowires extracted from their porous matrix cannot be measured; thus, this short cannot be avoided with today's technology. Mean free path limitations²⁰ increase the resistivity and affect zT negatively. Further, wires with diameters significantly below 10 nm display localization effects.¹⁸ This is understood readily from the Anderson-Ioffe-Regel criterion for band conduction: the product of the Fermi wavevector k_F and the mean free path ℓ must obey $k_F\ell > 1$. For electrons in Bi, k_F is highly anisotropic, as shown by de Haas–van Alphen and Shubnikov–de Haas measurements,⁹ and show a lower bound of $k_F \approx 1 \times 10^8 \text{ m}^{-1}$. Assuming that the wire diameter limits ℓ , localization is expected to appear for diameters around $k_F^{-1} \approx 10 \text{ nm}$, as observed. In hindsight, this limits the applicability range of the early theoretical predictions.

Dresselhaus and co-workers suggested studying quantum wells,²¹ nanowires, and nanocomposites of $\text{Bi}_{1-x}\text{Sb}_x$ alloys. Sb is isoelectronic with Bi, and the alloys are solid solutions throughout the concentration range with no change in space group ($\bar{3}m$). Alloying Sb into Bi has three principal effects on its *bulk* band structure: with increasing Sb content, (i) the direct energy gap $E_{g\text{Lsa}}$ closes and ultimately inverts, (ii) the T-point hole band decreases in energy vis-à-vis the L-point bands, and (iii) the H-point VB increases in energy vis-à-vis the L-point bands.²²

Bulk single-crystal semiconducting $\text{Bi}_{1-x}\text{Sb}_x$ alloys yield the highest zT of all n-type materials at cryogenic temperatures when the fluxes are oriented along the trigonal axis.^{23,24} Potassium is a resonant dopant in Bi and its alloys; a record $zT = 0.7$ was reported²⁵ at 100 K on K-doped $\text{Bi}_{95.5}\text{Sb}_{4.5}$, a composition near where the L-point bands have the Dirac dispersion. That sample yields $zT > 0.5$ from 40 to 300 K. P-type $\text{Bi}_{1-x}\text{Sb}_x$ alloys generally have lower zT values than n-type alloys, despite that Ga is a resonant acceptor in the material.²⁶ While the best materials still are single crystals, the best p-type materials zT values are obtained when the fluxes are oriented in the trigonal plane.²⁷ $\text{Bi}_{97}\text{Sb}_3$ is also one of the alloys best suited for Ettingshausen coolers²⁸. Most bulk alloys give slightly better TE performance in Peltier and Ettingshausen geometries when the electron concentration is lowered by light p-type counter doping.²⁹

The Dresselhaus group calculated size-quantization effects in $\text{Bi}_{1-x}\text{Sb}_x$ alloys for quantum wells³⁰ and wires.³¹ size quantization and alloying effects cooperate to increase energy gaps. As a result, the semimetal-semiconductor transition occurring in 49 nm-diameter wires of elemental Bi or 9 at.% Sb in bulk $\text{Bi}_{1-x}\text{Sb}_x$ alloys occurs at lower Sb concentrations in nanostructures, or at larger diameters in $\text{Bi}_{1-x}\text{Sb}_x$ than in Bi. The calculated (diameter, composition) phase diagrams are reported in Refs. [30,31]. By adding Sb to Bi, one can reasonably hope to increase the thermopower by size quantization in quantum wires of diameters substantially larger than the limit where localization effects occur. The present manuscript aims to show this experimentally.

The Dresselhaus group pioneered the first experiments on 65 nm- and 40 nm-diameter $\text{Bi}_{1-x}\text{Sb}_x$ ($x=0.05\text{--}0.10$) nanowires by using high-pressure injection synthesis,³² but they observed a more modest Seebeck coefficient enhancement than predicted, and the total thermopower remained significantly lower than single-crystal bulk alloys along the trigonal direction,²⁹ reaching only $-60 \mu\text{V/K}$ (100–300 K) for 45 nm $\text{Bi}_{0.95}\text{Sb}_{0.04}$ wires. The in-situ vapor-deposition

method was applied successfully to other elements, such as Sb³³ and Zn³⁴, but was unsuccessful preparing Bi_{1-x}Sb_x alloy nanowires due to the large vapor pressure difference between Bi and Sb.

2. Experimental

Here, we report on a new, wet-chemical synthesis route to prepare Bi_{1-x}Sb_x nanowires that show enhanced thermopower compared to polycrystalline equivalent alloys. The synthesis and characterization of elemental Bi nanowires using the same route as is used here for Bi-Sb alloys is described in detail in Ref. [35], and the same reference contains TEM analysis of Bi nanowires and transport measurements on elemental Bi nanowire composites, which are extended here to Bi-Sb/silica composites. In particular, temperature-dependent Hall measurements on a Bi nanowire/silica composite indicates a carrier concentration that increases as in an intrinsic semiconductor, with an energy gap of 45 meV, which corresponds quite well with the prediction of the Dresselhaus group¹¹ for 20 nm nanowires.

The wet-chemistry synthesis route given here applies to Bi_{1-x}Sb_x alloy nanocomposites. Since these materials undergo a last heat treatment far below their melting point, they have a lower mobility than ingot-cast samples. Therefore, a comparison is made first between the galvanomagnetic (resistivity, Hall effect), thermomagnetic (Seebeck and Nernst coefficients), and thermal (thermal conductivity) properties of bulk Bi_{1-x}Sb_x alloys synthesized via the conventional melt-casting process and those made by the wet-chemistry method used in the synthesis of the nanocomposites. The results of the latter are then compared in the next section to similar measurements on chemically synthesized nanocomposites. We report a clear enhancement of the thermopower in nanowire composites of Bi₉₄Sb₆, at high temperature (250 – 400 K). This is particularly interesting because, in the existing literature, neither Sb content nor even extrinsic doping of Bi with acceptor or donor impurities is reported to affect the room

temperature thermopower of either Bi or Bi-rich Bi-Sb alloys significantly. These data indicate that size confinements alter that in a particularly meaningful way, implying that size-quantization effects influence that band structure.

2.1. Materials

Hydrochloric acid trace metal grade (36 wt%), 98% methanol, and 99% n-butanol were purchased from Sigma Aldrich. 99.999% bismuth(III) oxide, 99.999% antimony(III) oxide, 99% hydrazine monohydrate, and 99% n-octane were purchased from Alfa Aesar. 65 wt% trace metal grade nitric acid was obtained from Fisher Scientific. Elemental bismuth and antimony with 99.999% purity were obtained from 5N Plus. All reagents were used as received.

2.2. Synthesis

2.2.1. Bulk polycrystalline $\text{Bi}_{1-x}\text{Sb}_x$ compounds by ingot casting/quenching

A series of $\text{Bi}_{1-x}\text{Sb}_x$ bulk polycrystalline samples with $x = 0.03, 0.04, 0.05$, and 0.06 were prepared with a melting-quenching procedure. Bulk 99.999% Bi and 99.999% Sb were weighed to stoichiometry and approximately 10 g of material was loaded into a quartz ampoule. The ampoule was then sealed under vacuum and heated in a furnace at $800\text{ }^{\circ}\text{C}$ for 8 hours, with frequent shaking. Subsequently, the melts were cooled to $350\text{ }^{\circ}\text{C}$, followed by quenching in water to minimize phase segregation. For transport measurement, the as-quenched ingots were cut into parallelepipeds with dimensions of about $7 \times 2 \times 1.5\text{ mm}^3$ using a diamond saw.

2.2.2. Bulk polycrystalline $\text{Bi}_{1-x}\text{Sb}_x$ compounds by wet-chemistry route

Bulk $\text{Bi}_{1-x}\text{Sb}_x$ samples with $x = 0.02, 0.04$, and 0.10 were prepared by dissolving appropriate amounts of Bi_2O_3 and Sb_2O_3 in 36 v% hydrochloric acid and subsequently hydrolyzing the obtained precursor solution in distilled water. The precipitate was collected through filtration and dried at room temperature. Next, the Bi-Sb precursor was reduced to

remove all oxygen and chloride from the precursor at 230 °C for 12 h in a flow of hydrazine vapor carried by N₂ - 5% H₂ gas. During the low temperature reduction treatment of the precursor a mixture of elemental Bi, Sb and Bi-Sb phase were obtained. Bi_{1-x}Sb_x samples were obtained by sintering the Bi-Sb powders at 245 °C for 90 min at 30 MPa under vacuum using a spark plasma sintering (SPS) device. The compacted discs were cut into parallelepipeds with dimensions of approximately 7 × 2 × 1.5 mm³ using a diamond saw for transport measurements.

2.2.3. *Bi_{1-x}Sb_x nanocomposites by wet-chemistry route*

Bi_{1-x}Sb_x nanowire composite samples with $x = 0.03$ and 0.06 were prepared according to the process depicted in Fig. 1. First, the pores of a mesoporous silica template were impregnated with a mixture of bismuth and antimony salts, followed by the reduction of the salts to remove all Cl and O, yielding a mixture of elemental Bi, Sb and Bi_{1-x}Sb_x. Next, the nanocomposite powder was mixed with bulk Bi₈₈Sb₁₂, which promotes sintering while simultaneously acting as a resistive matrix by filling the voids between adjacent silica grains and presenting an energy gap much larger than that of the $x = 0.03$ or 0.06 material. Finally, bulk-sized samples composed of Bi_{1-x}Sb_x nanowires were obtained by sintering the nanocomposite powder using an SPS device.

The mesoporous silica template, pore-expanded FDU-12 (Fudan University-type mesoporous materials), was synthesized according to Ref. [36], while SBA-16 (Santa Barbara Amorphous-type material) was prepared as reported in Ref. [37]. The amounts of precursor impregnated into the template's pores were based on the quantities of precursor required to fill the pores completely with BiCl₃ and SbCl₃. Typically, an excess of precursors were added since the BiCl₃ precursor salt decomposes to denser BiOCl during the impregnation, allowing a higher pore filling with BiOCl compared to BiCl₃. As a reference, when the pores are filled completely with BiCl₃, the reduced samples can yield up to 32 v% Bi nanowires within the template's pores,

1 whereas that value can be as high as 60 v% when the pores are completely filled with BiOCl.
2 After filling the pores with Bi₉₄Sb₆ or Bi₉₇Sb₃ precursor, the nanocomposite powders were mixed
3 with 10 to 25 v% bulk polycrystalline Bi₈₈Sb₁₂. The continuous-feed nanocasting process used to
4 impregnate the template's pores with an aqueous precursor solution is detailed in Ref. [35]. A
5 schematic of the setup is shown in Fig. 2.

6 In a typical synthesis of Bi₉₄Sb₆ nanocomposites, 1 g FDU-12 mesoporous silica powder
7 with a BJH pore volume of 0.9 cm³/g and a pore diameter of approximately 15-25 nm was
8 dispersed in 100 mL octane and brought into a 250 mL perfluoroalkoxy alkane polymer (PFA)
9 round-bottom flask equipped with a Dean Stark separator and condenser. The recipient was
10 heated to 165 °C to enable the solvent to reflux gently. The Bi₉₄Sb₆ precursor solution was
11 prepared by dissolving 5.8646 g Bi₂O₃ (12.6 mmol) and 0.2342 g Sb₂O₃ (0.8 mmol) in 21 mL 36
12 w% hydrochloric acid and diluting with 5 mL water, 13 mL formic acid, and 120 mL methanol.
13 The solution was injected into the PFA flask at a rate of 4 mL/h using a syringe pump. The
14 template's pores were considered completely filled upon the addition of an excess of 200%
15 Bi₉₄Sb₆ precursor solution, based on the supposition that the addition of any further precursor
16 solution would lead only to deposition of precursor salt on the template's exterior surface. The
17 voids between the Bi₉₄Sb₆/silica grains were filled deliberately with a resistive matrix of Bi₈₈Sb₁₂
18 by adding an excess of Bi₈₈Sb₁₂ precursor solution. As the template's pores already were filled
19 with the Bi₉₄Sb₆ precursor, it was assumed that the Bi₈₈Sb₁₂ precursor was deposited on the
20 Bi₉₄Sb₆/silica grains' exterior surface. The amount of Bi₈₈Sb₁₂ accounted for 10 v% of the total
21 volume.

22 Bi₉₇Sb₃ nanocomposites were synthesized using SB-16 mesoporous silica template with a
23 pore diameter between 25 and 35 nm and a pore volume of 1.3 cm³/g. An excess of 160%

precursor salt was impregnated into the template, consisting of 6.8101 g Bi_2O_3 , 0.2720 g Sb_2O_3 , 25 mL 36w% HCl, 25 mL H_2O , and 25 mL formic acid, while 25 v% $\text{Bi}_{88}\text{Sb}_{12}$ matrix was added (4.7848 g Bi_2O_3 and 0.4082 g Sb_2O_3).

The as-synthesized nanocomposite powders were collected through filtration, washed with hexane, and subjected to the reduction treatment discussed earlier for bulk wet-chemistry synthesized $\text{Bi}_{1-x}\text{Sb}_x$. Bulk nanocomposite samples were formed by SPS sintering the powders as mentioned above. Note that all processes, including cutting the sample, sample mounting and transport measurements, were conducted under air-free conditions to prevent any oxidation of the nanowires.³⁵

2.4 Characterization

X-ray powder diffraction (XRD) (Fig. 3) patterns were recorded on a Rigaku Miniflex Diffractometer with the Bragg–Brentano theta-2 theta configuration and using $\text{Cu K}\alpha$ radiation. Nitrogen sorption experiments were performed at 77 K with a Micromeritics TriStar 3000 device. Samples were vacuum dried at 180 °C for 12 h prior to analysis. The pore-size distribution, and consequently the pore diameter, was determined by analysis of the adsorption branch of the isotherms using the Barrett, Joyner, and Halenda method (BJH, procedure for calculating pore size distributions from experimental isotherms using the Kelvin model of pore filling). X-ray fluorescence (XRF) measurements were performed on a Rigaku NEXCG device. The sample compositions were analyzed by dissolving small pieces of samples into 3:1 hydrochloric acid–nitric acid. The recorded intensities were related to their composition using a calibration curve.

Galvanomagnetic and thermomagnetic properties (including thermopower, resistivity, Hall coefficient, and Nernst coefficient) were measured in a self-built cryostat from 80 K to 400 K using the method described in Ref. [38]. Thermal conductivity was measured using a steady-state heat-sink method. Mobility is calculated from the measured resistivity and Hall coefficient. The error in the thermopower mainly results from electrical noise in voltage and thermocouples because the mounting ensures that the temperature and voltage differences are measured at the same point. Two copper-constantan thermocouples were attached to the sample with silver epoxy; the attachment spot was made intentionally small to minimize error in the thermopower measurement, estimated to be $\sim 3\%$. The errors in the resistivity, Hall coefficient and Nernst coefficient mainly come from geometric uncertainties. The error in the Hall coefficient and Nernst coefficient is estimated to be 5% and the error in resistivity 10%. The error in thermal conductivity comes from 2 sources: geometric uncertainty and radiation heat loss, which is measured in a cryostat without the sample as a function of temperature. The samples have a relatively high thermal conductivity, and the measurements are cut off at the temperature at which it is estimated that the radiation loss is $\sim 10\%$ of the sample conductance. To this, one adds the geometric uncertainty of also $\sim 10\%$. Note that the geometric uncertainty in thermal conductivity and in electrical resistivity will compensate each other when calculating zT .

3. Galvanomagnetic and thermomagnetic data

In this section, the galvanomagnetic and thermomagnetic properties of cast ingots and of wet-chemistry-prepared $\text{Bi}_{1-x}\text{Sb}_x$ alloys are compared. Fig. 4 (a) shows the temperature-dependence of the resistivity of bulk polycrystalline cast ingots of $\text{Bi}_{1-x}\text{Sb}_x$ with $x=3, 4, 5$, and 6 at.%, which are quite similar to the average of results obtained in the literature^{23,24} along the binary and trigonal axes. The chemically prepared polycrystals in Fig. 4 (b) for $x = 2, 4$, and 10

at.% are more resistive by a factor of ~ 2 at room temperature, and more at 100 K. The results on the nanowire composites of diameter around 15-25 and 25-35 nm for $x = 3$ and 6 at.% are another factor of ~ 5 more resistive. However, we note that the resistivity is measured using the physical dimensions of the composite, and is not corrected for the volume fraction of the Bi-Sb material in it. Given that Bi-Sb fills in only about 35v% of the template's pore volume, while the rest (SiO_2 and voids) does not conduct, roughly a factor of 2 from the total increase in resistivity is simply due to the geometric effect.

To analyze further the origin of these temperature dependences, low-field (i.e. at field where the product of mobility and magnetic induction is below unity, $\mu B < 1$) Hall effect data are taken. For the nanocomposites, the Hall resistivity is corrected for the volume fractions of Bi-Sb by using the effective medium theory³⁹ for the Hall effect; for a 35% Bi-Sb filling by volume, that correction is a factor of 2. It is known that the Hall and magnetoresistance data of elemental Bi are the result of the contributions of both electrons and holes, necessitating a complicated fit to obtain electron and hole concentrations and mobilities separately.⁴⁰ However, the semiconducting Bi-Sb alloys can, in principle, be treated as a single, n-type carrier system, and the carrier concentration then becomes the inverse of the Hall constant R_H times the electron charge e . This quantity is represented in Fig. 5 for samples of a composition such that they are semiconducting. The carrier concentration increases monotonically with temperature, the classical behavior of narrow-gap semiconductors, and the model should hold at least up to 150-200 K, given the projected values for the band gaps. From this and the resistivity in Fig. 4, one can derive the electron mobilities in the different samples, which are reported in Fig. 6. The mobility of the bulk ingots at liquid N_2 temperature is roughly 50% higher than that of the bulk samples prepared by wet chemistry and become comparable around room-temperature; that of

the nanowire composites are approximately one order of magnitude lower than bulk samples prepared by wet chemistry. For the resistivity, a factor of 2 of that ratio is due to geometry alone (a calculation of the purely geometric effects based on the effective medium theory is presented in the supplement¹).

In the high-temperature regime where $d\rho/dT > 0$, the temperature dependence of the resistivity is due to the decrease in mobility with increasing temperature, an indication of the presence of electron-acoustic phonon scattering over the increase in electron concentration. In the temperature range where $d\rho/dT < 0$, the temperature dependence of the resistivity is dominated by the increase in carrier concentration, presumably by thermal excitations of the carriers across the energy gap.

The total thermal conductivity is shown in Fig. 7. For the bulk ingots, the order of magnitude of the electronic contribution can be estimated from the Wiedemann-Franz-Lorenz law, using the free-electron Lorenz number, to be of the order of 2 W/mK at 100 K and > 4 W/mK at 300 K. For the bulk samples prepared with wet-chemical methods, values > 3 W/mK are estimated at 300 K, but much less for the 4 and 10% Sb samples at 100 K. It is known that ambipolar conduction dominates the thermal conduction in semimetallic Bi at 200 K.¹⁰ The samples studied here are narrow-gap semiconductors, so that the ambipolar conduction should be much lower, but it cannot be dismissed at the temperatures where the samples essentially become intrinsic semiconductors. Separating the ambipolar term requires knowledge of the partial conductivities and thermopowers of both electrons and holes, for which we have too few data in polycrystals (Ref. [10] used single crystals of two separate orientations, together with assumptions about the band structure.) It is clear from the numbers above that the thermal conductivity of the bulk ingots at all temperatures, and that of the 4 and 10% Sb ingots prepared

by wet chemistry at 300 K, has a very substantial electronic contribution. The thermal conductivity of the nanowire composites remains nearly temperature independent at 2 W/mK. Since that of the SiO_2 is of the order of 0.2 W/mK, and the Bi-Sb fills about 35 v% of the sample, it appears that the thermal conductivity of the Bi-Sb in the pores dominates the measured values. The thermal short through the porous host material, which had affected the zT of nanowire array samples in the past¹⁹, is apparently less of a problem in this material. This is probably because the fraction of the pores filled by Bi-Sb nanowires that are electrically in contact with each other is much improved by the present wet-chemical method and by the multiple connectivity of the host material's channels.

Most interesting are the thermopower results, given in Fig. 8. It is known that the thermoelectric power of elemental Bi¹⁰ and of the semimetallic $\text{Bi}_{1-x}\text{Sb}_x$ alloys²³ is anisotropic, with the thermopower along the c-axis $\alpha_{//}$ as much as twice the in-plane thermopower α_{\perp} . In contrast, the thermopower of the semiconducting alloys ($x = 12, 15$ and 18 at.%)²³ is more isotropic. Since this manuscript concerns polycrystals, it is assumed that the thermopower α shown in Fig. 8 is an average given by $\alpha = \frac{2}{3}\alpha_{\perp} + \frac{1}{3}\alpha_{//}$. The thermopower reported for the cast ingots and the bulk samples prepared by wet chemistry all follow the values reported in the literature²³ for their respective values of x . The low-temperature value reported for $x = 0.1$ (Fig. 8b) is the highest reported here, but also quite usual at that concentration.²³ Generally, as the temperature increases to and above room temperature, the thermopower of all samples converge to a value between -50 and -80 $\mu\text{V/K}$, probably because $k_B T$ approaches the energies of the details of $E_{gLs\alpha}(T)$, $E_{gTLs}(T)$, and $E_{gTL\alpha}(T)$.

In contrast, the thermopower of the 20 nm-diameter nanocomposite sample of $\text{Bi}_{96}\text{Sb}_6$ maintains a thermopower with an absolute value in excess of 100 $\mu\text{V/K}$ from 300 to 380 K (see

Fig. 8b). A comparison of the thermopower of this polycrystalline sample with literature values, given in Fig. 8c, shows that, to the best of our knowledge, this value has not been equaled previously by Sb-alloying of Bi alone. This change in thermopower also cannot result from an effective medium effect, which is calculated in the supplement.¹ The sample has a quite high carrier concentration (2 to $3 \times 10^{19} \text{cm}^{-3}$) and mobility (200 to $100 \text{ cm}^2/\text{Vs}$) in that temperature range, indicating band conduction. The thermopower is also much larger than what can be achieved with $\text{Bi}_{88}\text{Sb}_{12}$, indicating that the effect cannot be due to the material in the channels between the nanowires. Therefore, we suggest that size quantization increases the gap of this material above what is possible with Sb alloying.

The Nernst effect is typically larger than the Seebeck effect at moderate magnetic fields (i.e. $\mu\text{B} \sim 1$) in semimetals⁴¹ in general and in Bi in particular,⁴² because the contributions of electrons and holes are additive. The low-field adiabatic Nernst coefficients N (i.e. the slope of the transverse thermopower with field) of the alloys measured here are given in Fig. 9 and generally confirm the conclusions. N decreases as x is increased, but is generally quite large with $N \times 1 \text{ T} > |\alpha|$ at 100 K (specifically $N \times 1 \text{ T} \sim 350$ to $100 \mu\text{V/K}$ whereas $\alpha \sim -50$ to $-120 \mu\text{V/K}$) in semimetallic samples for $x < 0.08$, while the reverse is true at $x = 0.1$. The exceptions are the nanowire composites, which behave like the semiconducting samples.

The thermoelectric power factor $PF \equiv \alpha^2/\rho$ and figure of merit $zT \equiv \alpha^2 T/\rho\kappa$ are calculated from the above data and reported in Figures 10 and 11, respectively. It is known^{23,24} that power factors of the bulk single-crystal $\text{Bi}_{1-x}\text{Sb}_x$ alloys along the trigonal direction reach $100 \mu\text{W/cm K}^2$, far exceeding those of the tetradymites.² The present results extend that to polycrystals. The relatively lower zT of $\text{Bi}_{1-x}\text{Sb}_x$ alloys compared to tetradymites are due to their high lattice thermal conductivity and modest Seebeck coefficient. The fact that the present

samples are polycrystals is a second major disadvantage inherent in nanocomposites, since, as outlined in the introduction, the best zT (≤ 0.7) values are achieved in trigonal crystals doped with the resonant impurity potassium. However, from a practical standpoint, polycrystalline samples are preferred over single crystals since they are mechanically stronger and easier to synthesize. In addition, the values obtained for the nanowire composites in Fig. 10 are orders of magnitude better than those measured on previous Bi nanocomposites.¹⁹ According to calculations by Rabin et al.,⁴³ n-type $\text{Bi}_{85}\text{Sb}_{15}$ nanowires with a diameter of 20 nm have the potential to reach zT values as high as 2.5, which would drastically enhance the efficiency of thermoelectric solid-state cooling devices and make them competitive with vapor-compression based cooling systems. However, Cornett et al.⁴⁴ reported that the extent of the zT enhancement in nanowire thermoelectrics also depends on single-band versus multi-subband transport, which previously was not considered and makes the expected zT arguable.

Conclusions

The wet-chemical method presented here enables the preparation of nanowire composites of semiconducting $\text{Bi}_{1-x}\text{Sb}_x$ alloys that previous nanowire impregnation methods (vapor deposition and high-pressure liquid injection) could not. Both a reduction of the nanowire diameter and the increase of Sb concentration x (up to 18%) are ways to potentially transform the semimetal Bi into a thermoelectrically relevant Te-free semiconductor. In the present work, both effects are used together. The work shows experimentally that 300 K thermopower values can be obtained in 20 nm $\text{Bi}_{94}\text{Sb}_6$ nanowire composites that exceed the thermopower of bulk polycrystals of any Sb concentration. Although smaller than the zT of single-crystals of Bi-Sb, and particularly ones resonantly doped with K, the zT values reported here are much improved over those obtained on nanocomposites in the past. This is because the wet-chemical method fills

1 the pores better than the vapor-deposition or high-pressure liquid injection methods. The
2 improvement comes from the fact that a much larger fraction of the Bi-Sb nanowires are in
3 electrical contact with one another in these composites than in those prepared in the past.¹⁹
4 Further research involves the optimization of the alloy composition and the carrier concentration
5 of the nanowires to maximize their zT .

6 7 **Acknowledgements**

8 The work was supported by the U.S. NSF grant EFRI-2DARE 1433467, as well as by IWT and
9 FWO grants, Flanders, Belgium. This original research was carried out in honor and memory of
10 Professor Mildred Spiewak Dresselhaus, 1930-2017, whose influence on the authors both
11 personally and professionally, was profound.

Figure captions

Fig. 1 Schematic representation of the synthesis procedure of bulk $\text{Bi}_{1-x}\text{Sb}_x$ nanowire composite samples, starting from the porous silica in (a). The different steps towards the end product consists of: (1) impregnation of the aqueous Bi-Sb precursor solution into the template's pores; (2) reduction of the Bi-Sb precursor to metallic Bi-Sb; (3) mixing of the nanocomposite powder with a resistive $\text{Bi}_{88}\text{Sb}_{12}$ matrix; and (4) SPS sintering of the nanocomposite powder into a bulk sized sample. The different intermediate products are: (a) mesoporous silica grain with tuneable pore diameters from 2 to 50 nm, a typical density of 30%, and an interconnected pore structure that allows better percolation between the nanowires; (b) mesoporous silica with a mixture of BiCl_3 and SbCl_3 deposited in the pores; (c) mesoporous silica with metallic Bi-Sb inside it's pores; (d) Bi-Sb nanowire composite mixed with $\text{Bi}_{88}\text{Sb}_{12}$ matrix; and (e) bulk sized sample containing nanowires embedded in the silica pores. Note that Bi-Sb leaches partially outside the pores during the reduction treatment, which is shown in (c). To help with sintering while minimizing the effects of electrical short circuits through the leached material, a resistive matrix of $\text{Bi}_{88}\text{Sb}_{12}$ was added.

Fig. 2 Continuous-feed nanocasting setup used to impregnate the mesoporous silica's pores. The setup consists of a heating plate, a round-bottom flask, a Dean Stark separator, an addition system, such as a syringe pump, and a condenser. The silica template and n-octane are brought into the PFA flask and connected with the Dean Stark separator and the addition system. First, the temperature is increased to 165 °C, allowing the non-polar solvent to boil. Second, the precursor solution is added at a rate of 4 mL/h and infiltrates the pores through capillary impregnation. Next, the immiscible aqueous phase is separated from the n-octane based on

1 difference in density. Consequently, the process allows the deposition of BiCl_3 and SbCl_3 metal
2 salts inside the template's pores, starting from a diluted precursor solution.

3
4 **Fig. 3** Normalized X-ray powder diffraction (XRD) patterns of (a) the Bi-Sb precursor embedded
5 in the silica template, (b) the reduced samples, and (c) SPS sintered samples. (a) Upon
6 impregnating the mesoporous silica template with a mixture of BiCl_3 and SbCl_3 , the precursor
7 salts hydrolyzed with the formation of BiOCl . Neither SbCl_3 nor SbOCl were detected, which
8 may be due to low content or their presence as an amorphous phase or phases. (b) The reduced
9 samples were obtained by treating the powders at 230 °C in a flow of N_2 , 5% H_2 saturated with
10 hydrazine hydrate vapor for 12 h. The diffraction peaks of elemental Bi and Sb can be observed
11 as indicated on the figure. (c) $\text{Bi}_{1-x}\text{Sb}_x$ alloys were formed during the SPS sintering process at
12 245 °C for 90 min as can be seen from the shift in 2Theta values and absence of elemental Sb. 10
13 w% Si was added as internal standard to confirm the peak shift was due to alloying.

14
15 **Fig. 4** Temperature dependence of the resistivity of (a) polycrystalline cast ingots of $\text{Bi}_{1-x}\text{Sb}_x$
16 alloys of the compositions indicated. Frame (b) shows the same quantity measured on
17 polycrystals sintered from powders prepared using the same wet-chemistry as for the nanowire
18 composites. The latter are labelled as 20 nm-diameter nanowire (NW) composites of $\text{Bi}_{94}\text{Sb}_6$ and
19 30 nm-diameter NW composites of $\text{Bi}_{97}\text{Sb}_3$.

20
21 **Fig. 5** Temperature dependence of the inverse of the low-field Hall coefficient of (a)
22 polycrystalline cast ingots of semiconducting $\text{Bi}_{1-x}\text{Sb}_x$ alloys ($x > 0.04$) of the compositions
23 indicated. Frame (b) shows the same quantity measured on polycrystals sintered from powders

prepared using the same wet-chemistry as for the nanowire composites. The latter are labelled as 20 nm-diameter NW composites of $\text{Bi}_{94}\text{Sb}_6$ and 30 nm-diameter NW composites of $\text{Bi}_{97}\text{Sb}_3$.

Fig. 6 Temperature dependence of the electron mobility of (a) polycrystalline cast ingots of semiconducting $\text{B}_{1-x}\text{Sb}_x$ alloys ($x > 0.04$) of the compositions indicated. Frame (b) shows the same quantity measured on polycrystals sintered from powders prepared using the same wet-chemistry as for the nanowire composites. The latter are labelled as 20 nm-diameter NW composites of $\text{Bi}_{94}\text{Sb}_6$ and 30 nm-diameter NW composites of $\text{Bi}_{97}\text{Sb}_3$.

Fig. 7 Temperature dependence of the thermal conductivity of (a) polycrystalline cast ingots of $\text{B}_{1-x}\text{Sb}_x$ alloys of the compositions indicated. Frame (b) shows the same quantity measured on polycrystals sintered from powders prepared using the same wet-chemistry as for the nanowire composites. The latter are labelled as 20 nm-diameter NW composites of $\text{Bi}_{94}\text{Sb}_6$ and 30 nm-diameter NW composites of $\text{Bi}_{97}\text{Sb}_3$.

Fig. 8 Temperature dependence of the Seebeck coefficient of (a) polycrystalline cast ingots of $\text{B}_{1-x}\text{Sb}_x$ alloys of the compositions indicated. Frame (b) shows the same quantity measured on polycrystals sintered from powders prepared using the same wet-chemistry as for the nanowire composites. The latter are labelled as 20 nm-diameter NW composites of $\text{Bi}_{94}\text{Sb}_6$ and 30 nm-diameter NW composites of $\text{Bi}_{97}\text{Sb}_3$. Frame (c) compares the Seebeck coefficient of the 20 nm-diameter NW composites of $\text{Bi}_{94}\text{Sb}_6$ with values collected from the literature for the various Bi-Sb alloys labelled. The references are: YIM, 1972: Ref. [23]; Tanuma 1961: Ref. [45]; Lucas 2012: Ref. [46]

Fig. 9 Temperature dependence of the low-field Nernst coefficient of (a) polycrystalline cast ingots of $B_{1-x}Sb_x$ alloys of the compositions indicated. Frame (b) shows the same quantity measured on polycrystals sintered from powders prepared using the same wet-chemistry as for the nanowire composites. The latter are labelled as 20 nm-diameter NW composites of $Bi_{94}Sb_6$ and 30 nm-diameter NW composites of $Bi_{97}Sb_3$.

Fig. 10 Temperature dependence of the thermoelectric power factor of (a) polycrystalline cast ingots of $B_{1-x}Sb_x$ alloys of the compositions indicated. Frame (b) shows the same quantity measured on polycrystals sintered from powders prepared using the same wet-chemistry as for the nanowire composites. The latter are labelled as 20 nm-diameter NW composites of $Bi_{94}Sb_6$ and 30 nm-diameter NW composites of $Bi_{97}Sb_3$.

Fig. 11 Temperature dependence of the thermoelectric figure of merit zT of (a) polycrystalline cast ingots of $B_{1-x}Sb_x$ alloys of the compositions indicated. Frame (b) shows the same quantity measured on polycrystals sintered from powders prepared using the same wet-chemistry as for the nanowire composites. The latter are labelled as 20 nm-diameter NW composites of $Bi_{94}Sb_6$ and 30 nm-diameter NW composites of $Bi_{97}Sb_3$.

1 References

¹ See Supplemental Material at [URL will be inserted by publisher]. The supplement has two sections. In the first, we derive the condition under which active cooling (e.g. with a Peltier cooler) results in a mre compact heat exchange system than passive cooling, i.e. we derive Eq. (1). The second part gives effective medium calculations of the thermoelectric power.

Resistivity and thermal conductivity of te Bi-Sb / alumina composites.

² J. P. Heremans, R. J. Cava, and N. Samarth, Tetradymites as thermoelectrics and topological insulators, *Nature Reviews Materials* **2**, 17049 (2017), doi:10.1038/natrevmats.2017.49

³ AMS Alloy Phase Diagram Data Base, P. Villars, editor-in-chief; H. Okamoto and K. Cenzual, section editors, © 2006-2016 ASM International.

⁴ L. D. Hicks, and M. S. Dresselhaus, Effect of quantum-well structures on the thermoelectric figure of merit, *Phys. Rev. B* **47**, 12727 (1993).

⁵ L. D. Hicks, and M. S. Dresselhaus, Thermoelectric figure of merit of a one-dimensional conductor, *Phys. Rev. B* **47**, 16631 (1993).

⁶ M. Maltz, and M. S. Dresselhaus, Magnetoreflexion Studies in Bismuth, *Phys. Rev. B* **2**, 2877 (1970); M. P. Vecchi, and M. S. Dresselhaus, Magnetic energy levels of bismuth in the low-quantum-number limit, *Phys. Rev. B* **9**, 3257 (1974).

⁷ M. P. Vecchi, J. R. Pereira, and M. S. Dresselhaus, Anomalies in the magnetoreflexion spectrum of bismuth in the low-quantum-number limit, *Phys. Rev. B* **14**, 298 (1976).

⁸ M. P. Vecchi, and M. S. Dresselhaus, Temperature dependence of the band parameters of bismuth, *Phys. Rev. B* **10**, 771 (1974).

-
- ⁹ V. S. Edel'man, Properties of electrons in bismuth, Sov. Phys. Usp. **20**, 819 (1977), translated from Usp. Fiz. Nauk **123**, 257 (1977).
- ¹⁰ C. F. Gallo, B. S. Chandrasekhar and P. H. Sutter, Transport properties of bismuth single crystals, J. Appl. Phys. **34**, 144 (1963).
- ¹¹ Y. M. Lin, X. Sun, M. S. Dresselhaus, Theoretical investigation of thermoelectric transport properties of cylindrical Bi nanowires, Phys. Rev. B **62**, 4610 (2000).
- ¹² J. P. Heremans, M. S. Dresselhaus, L. Bell, and D. T. Morelli, Reflections on thermoelectrics, Nature Nanotechnology **8**, 471 (2013).
- ¹³ Z. Zhang, D. Gekhtman, M. S. Dresselhaus, and J. Y. Ying, Processing and characterization of single-crystalline ultrafine bismuth nanowires, Chem. Mater. **11**, 1659 (1999).
- ¹⁴ J. P. Heremans, C. M. Thrush, and D. T. Morelli, Enhanced thermoelectric power in bismuth nanocomposites, U.S. Patent Number 6670539; December 30, 2003.
- ¹⁵ J. P. Heremans, C. M. Thrush, Y. M. Lin, S. Cronin, Z. Zhang, M. S. Dresselhaus, J. F. Mansfield, Bismuth nanowire arrays: Synthesis and galvanomagnetic properties, Phys. Rev. B **61**, 2921 (2002).
- ¹⁶ Y. M. Lin, S. B. Cronin, J. Y. Ying, M. S. Dresselhaus, and J. P. Heremans, Transport properties of Bi nanowire arrays, Appl. Phys. Lett. **76**, 3944 (2000); doi: 10.1063/1.126829.
- ¹⁷ J. P. Heremans and C. M. Thrush, Thermoelectric power of bismuth nanowires, Phys. Rev. B **59**, 12579 (1999).
- ¹⁸ J. P. Heremans, C. M. Thrush, D. T. Morelli, Thermoelectric power of bismuth nanocomposites, Phys. Rev. Lett. **88**, 216801 (2002).
- ¹⁹ J. P. Heremans, Low-dimensional thermoelectricity, Acta Physica Polonica A **108**, 609 (2005).

-
- ²⁰ M. Murata, D. Nakamura, Y. Hasegawa, T. Komine, T. Taguchi, S. Nakamura, C. M. Jaworski, V. Jovovic, J. P. Heremans, Mean free path limitation of thermoelectric properties of bismuth nanowire, *J. Appl. Phys.* **105**, 113706 (2009).
- ²¹ S. Tang, and M. S. Dresselhaus, Phase diagrams of $\text{Bi}_{1-x}\text{Sb}_x$ thin films with different growth orientations, *Phys. Rev. B* **86**, 075436 (2012).
- ²² L. Fu and C.L. Kane, Topological insulators with inversion symmetry, *Phys. Rev. B* **76**, 045302 (2007).
- ²³ W. M. Yim and A. Amith, BiSb alloys for magneto-thermoelectric and thermomagnetic cooling, *Solid-State Electronics* **15**, 1141 (1972).
- ²⁴ B. Lenoir, M. Cassart, J.-P. Michenaud, H. Scherrer, and S. Scherrer, Transport properties of Bi-rich Bi-Sb alloys, *J. Phys. Chem. Solids* **57**, 89 (1996); B. Lenoir, A. Dauscher, X. Devaux, R. Martin-Lopez, I. Y. Ravich, H. Scherrer, and S. Scherrer, Proceedings of 15th International Conference on Thermoelectrics, 1996 unpublished, pp. 1-13.
- ²⁵ J. P. Heremans, H. Jin, Y. H. Zheng, S. J. Watzman, and A. Prakash, BiSb and spin-related thermoelectric phenomena, *Proc. SPIE* **9821**, 982117 (2016), <http://dx.doi.org/10.1117/12.2228758>; J. P. Heremans, and H. Jin, Thermoelectric and spin-caloritronic coolers: from basics to recent developments, *Proc. SPIE* **9765**, 976506 (2016).
- ²⁶ H. Jin, B. Wiendlocha, and J.P. Heremans, P-type doping of elemental bismuth with indium, gallium and tin: a novel doping mechanism in solids, *Energy Environ. Sci.* **8**, 2027 (2015).
- ²⁷ H. Jin, C. M. Jaworski, and J. P. Heremans, Enhancement in the figure of merit of p-type $\text{Bi}_{1-x}\text{Sb}_x$ alloys through multiple valence-band doping, *Appl. Phys. Lett.* **101**, 053904 (2012).

-
- ²⁸ K. Scholtz, P. Jandl, U. Birkholz, and Z. M. Dashevskii, Infinite stage Ettingshausen cooling in Bi-Sb alloys, *J. Appl. Phys.* **75**, 5406 (1994).
- ²⁹ P. Jandl, and U. Birkholz, Thermogalvanomagnetic properties of Sn-doped Bi₉₅Sb₅ and its application for solid state cooling, *J. Appl. Phys.* **76**, 7351 (1994).
- ³⁰ S. Tang and M. S. Dresselhaus, Phase diagrams of Bi_{1-x}Sb_x thin films with different growth orientations, *Phys. Rev. B* **86**, 075436 (2012).
- ³¹ S. Tang and M. S. Dresselhaus, Electronic phases, band gaps, and band overlaps of bismuth antimony nanowires, *Phys. Rev. B* **89**, 045424 (2014); S. Tang, M. S. Dresselhaus, Electronic properties of nano-structured bismuth antimony materials, *J. Mater. Chem. C* **2**, 4710 (2014).
- ³² Y-M. Lin, O. Rabin, S. B. Cronin, J. Y. Ying and M. S. Dresselhaus, Semimetal–semiconductor transition in Bi_{1-x}Sb_x alloy nanowires and their thermoelectric properties, *Appl. Phys. Lett.* **81**, 2403 (2002).
- ³³ J. P. Heremans, C. M. Thrush, Y-M. Lin, S. B. Cronin, and M. S. Dresselhaus, Transport properties of antimony nanowires, *Phys. Rev. B* **63**, 085406 (2001).
- ³⁴ J. P. Heremans, C. M. Thrush, D. T. Morelli, and M-C. Wu, Resistance, Magnetoresistance, and thermopower of zinc nanowire composites, *Phys. Rev. Lett.* **91**, 076804 (2003).
- ³⁵ K. Vandaele, J. P. Heremans, I. Van Driessche, P. Van Der Voort, and K. De Buysser, Continuous-feed nanocasting process for the synthesis of bismuth nanowire composites, *Chem. Comm.* **53**, 12294 (2017).
- ³⁶ L. Huang, X. Yan, and M. Kruk, Synthesis of Ultralarge-pore FDU-12 silica with face-centered cubic structure, *Langmuir* **26**, 14871 (2010).

-
- ³⁷ Z. Dongyuan, H. Qisheng, F. Jianglin, F. C. Bradley, and D. S. Galen, Nonionic triblock and star diblock copolymer and oligomeric surfactant syntheses of highly ordered, hydrothermally stable, mesoporous silica structures, *J. Am. Chem. Soc.* **120**, 6024 (1998).
- ³⁸ J. P. Heremans, C. M. Thrush, and D. T. Morelli, Thermopower enhancement in lead telluride nanostructures, *Phys Rev B* **70**, 115334 (2004).
- ³⁹ D. J. Bergman, and D. G. Stroud, High-field magnetotransport in composite conductors: Effective-medium approximation, *Phys. Rev. B* **62**, 6603 (2000).
- ⁴⁰ J. P. Heremans, and O. P. Hansen, Influence of non-parabolicity on intravalley electron-phonon scattering; the case of bismuth, *J. Phys. C: Solid State Phys.* **12**, 3483 (1979).
- ⁴¹ S. J. Watzman, T. M. McCormick, C. Shekhar, S.-C. Wu, Y. Sun, A. Prakash, C. Felser, N. Trivedi, and J. P. Heremans, Dirac dispersion generates large Nernst effect in Weyl semimetals, *arXiv:1703.04700* (2017).
- ⁴² J. H. Mangez, J-P. Issi, and J. P. Heremans, Transport properties of bismuth in quantizing magnetic fields, *J. P., Phys. Rev. B* **14**, 4381-5 (1976).
- ⁴³ O. Rabin, Y. Lin, M. S. Dresselhaus, Anomalous high thermoelectric figure of merit in $\text{Bi}_{1-x}\text{Sb}_x$ nanowires by carrier pocket alignment, *Appl. Phys. Lett.* **79**, 81 (2001)
- ⁴⁴ J. E. Cornett and O. Rabin, Thermoelectric figure of merit calculations for semiconducting nanowires, *Appl. Phys. Lett.* **98**, 182104 (2011).
- ⁴⁵ S. Tanuma, Thermoelectric power of bismuth-antimony alloys, *J. Phys. Soc. Japan* **16**, 2354 (1961).
- ⁴⁶ K. C. Lukas, Thermoelectric properties of Ho-doped $\text{Bi}_{0.88}\text{Sb}_{0.12}$, *J. Mater. Science* **47**, 5729 (2012).

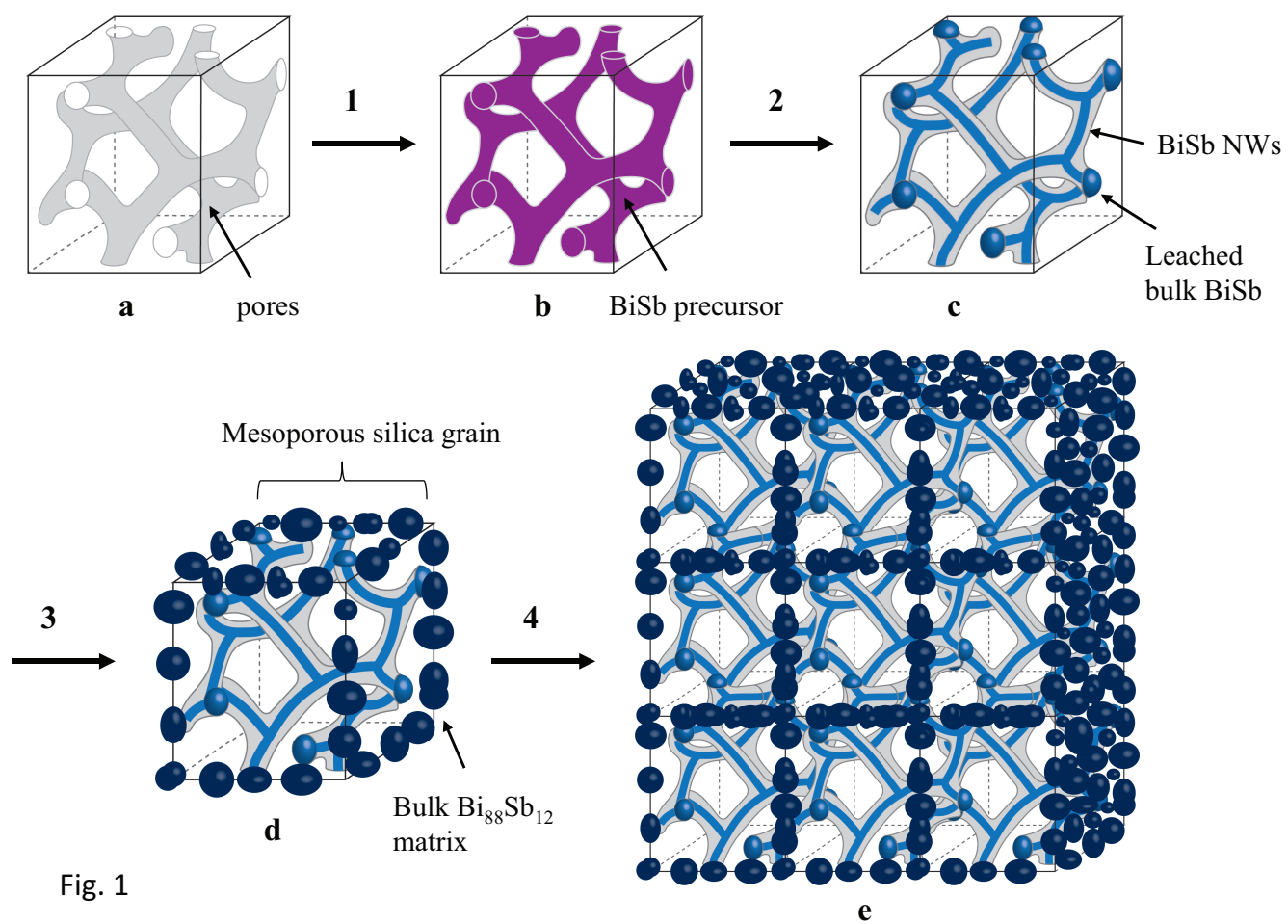


Fig. 1

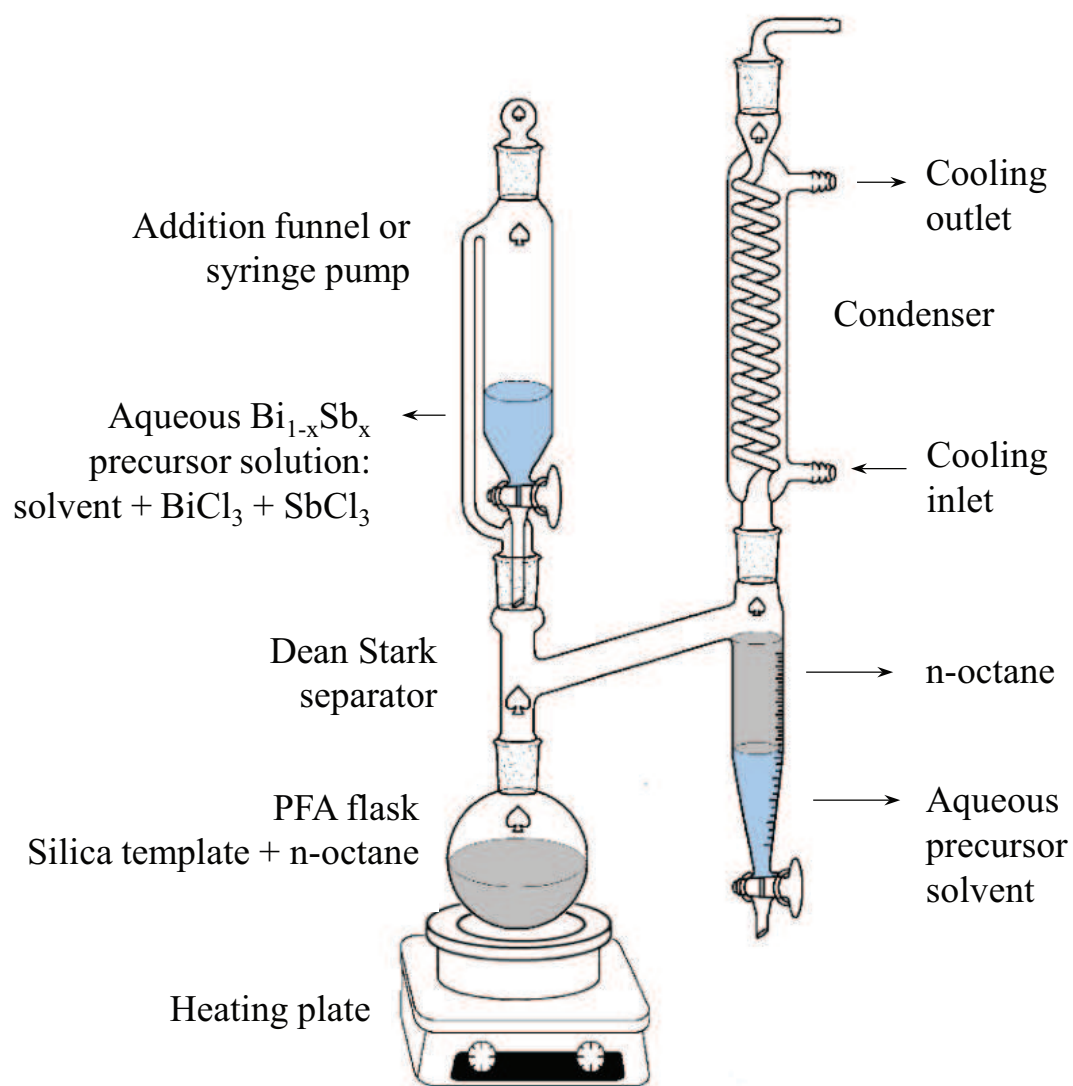


Fig. 2

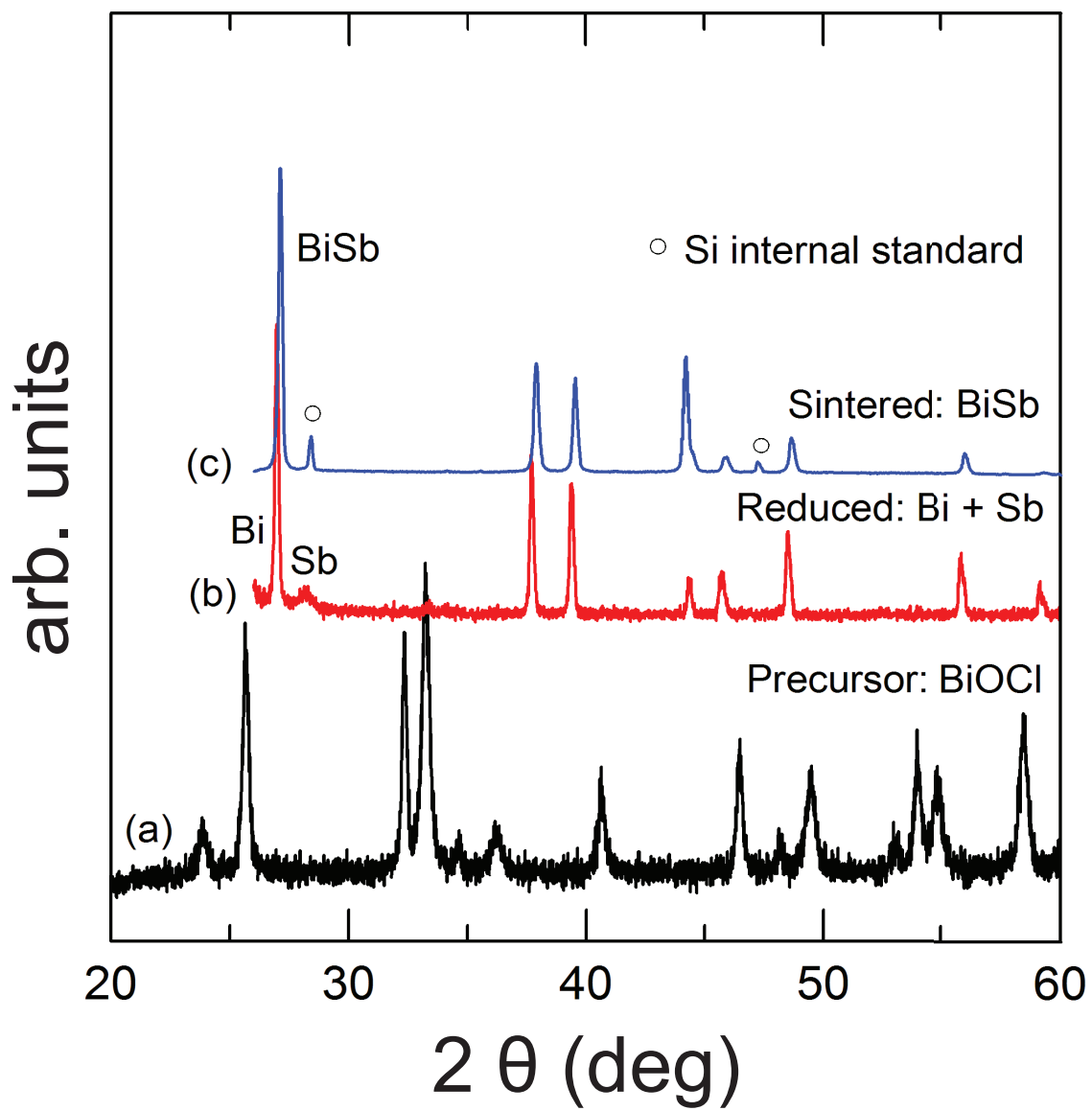


Fig. 3

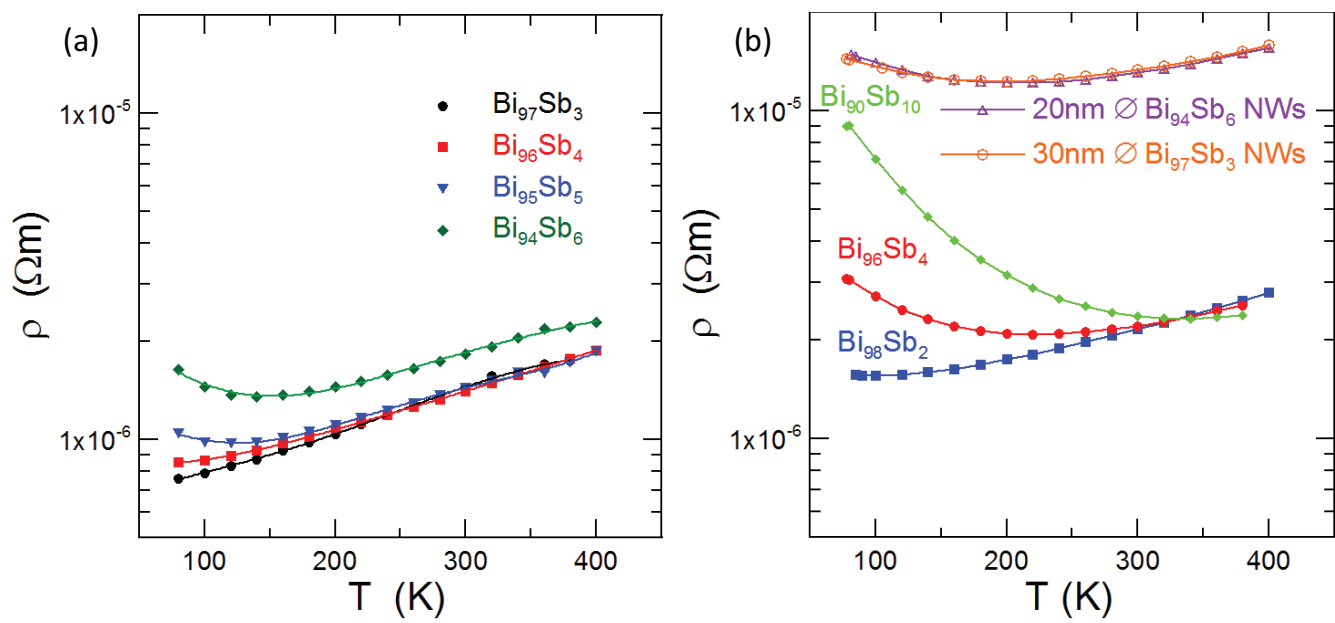


Fig. 4

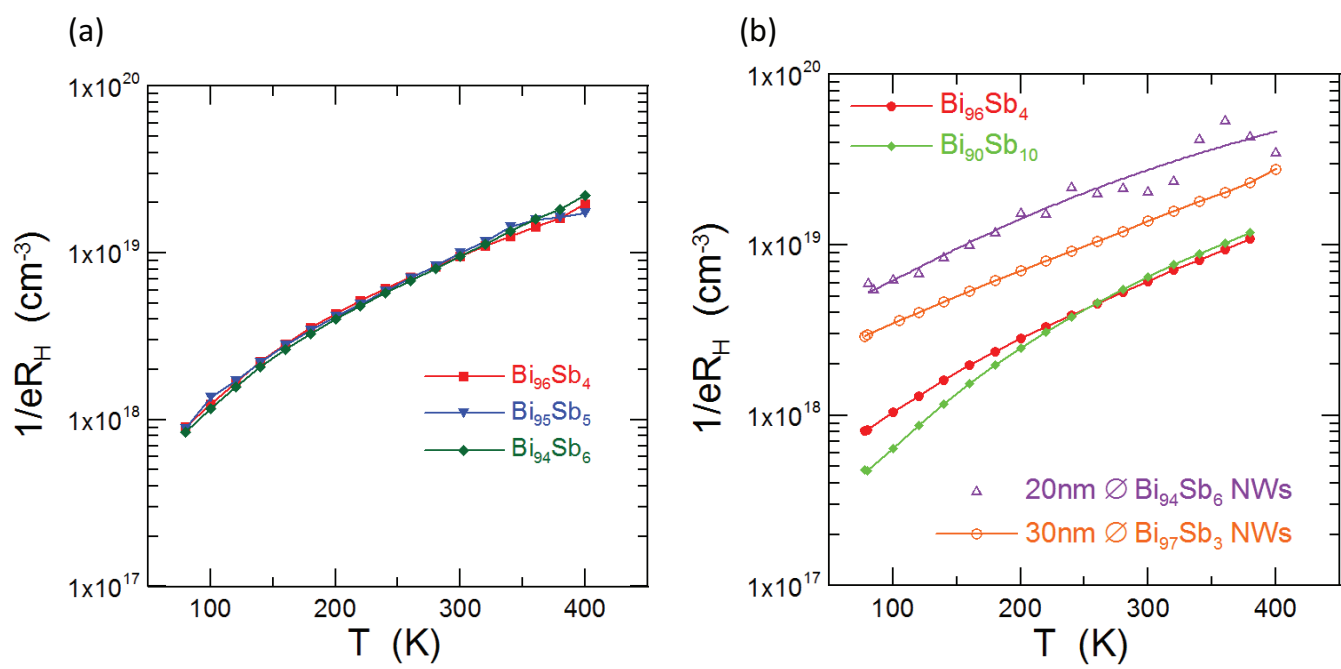


Fig. 5

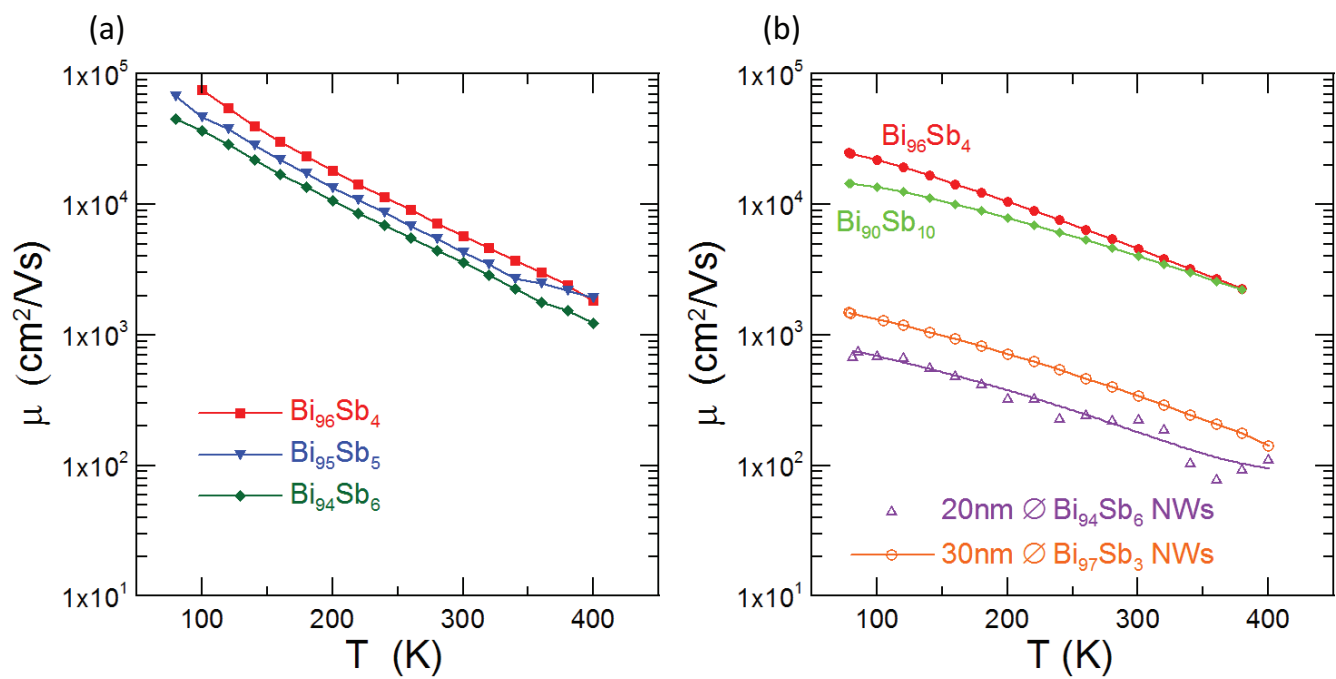


Fig. 6

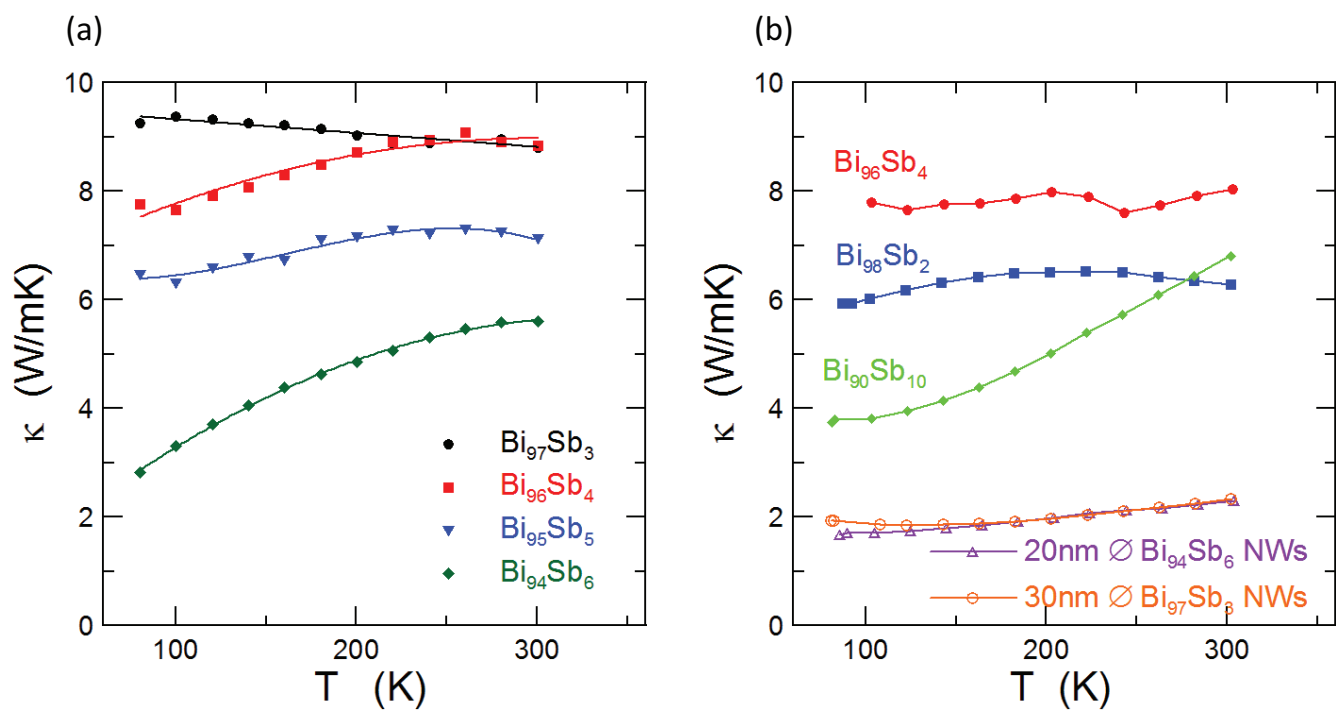


Fig. 7

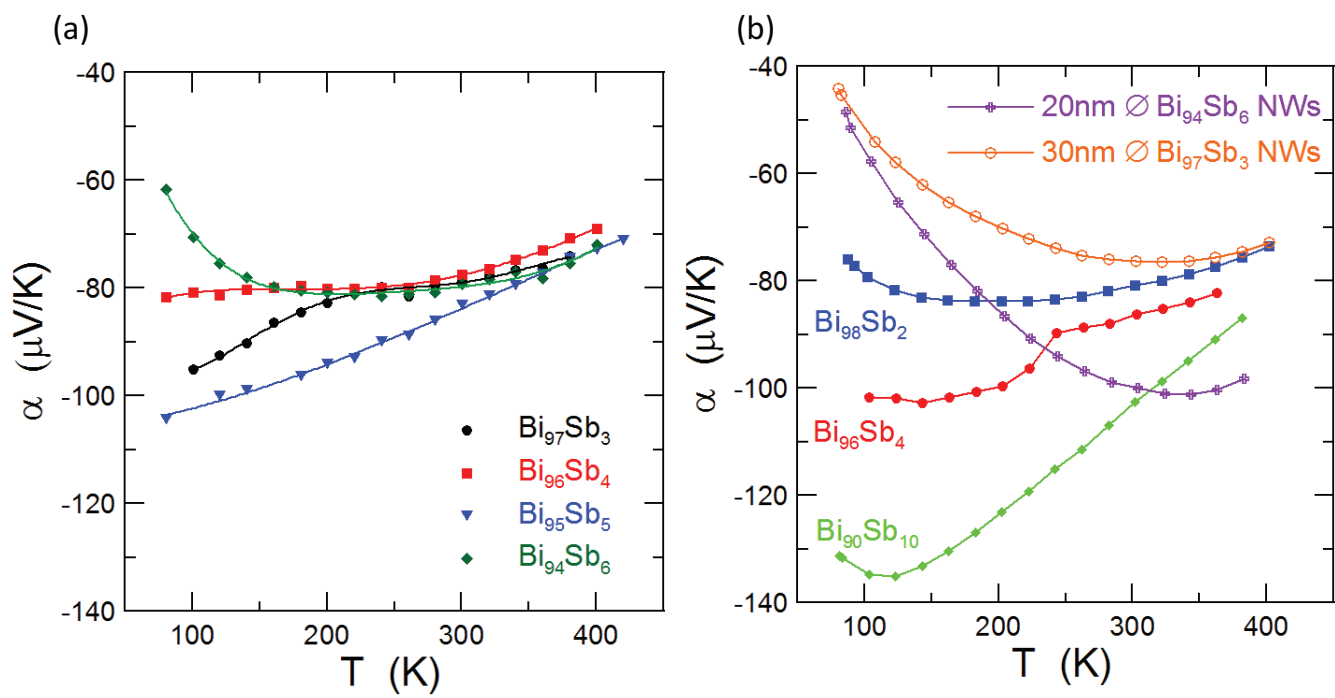


Fig. 8 (a,b)

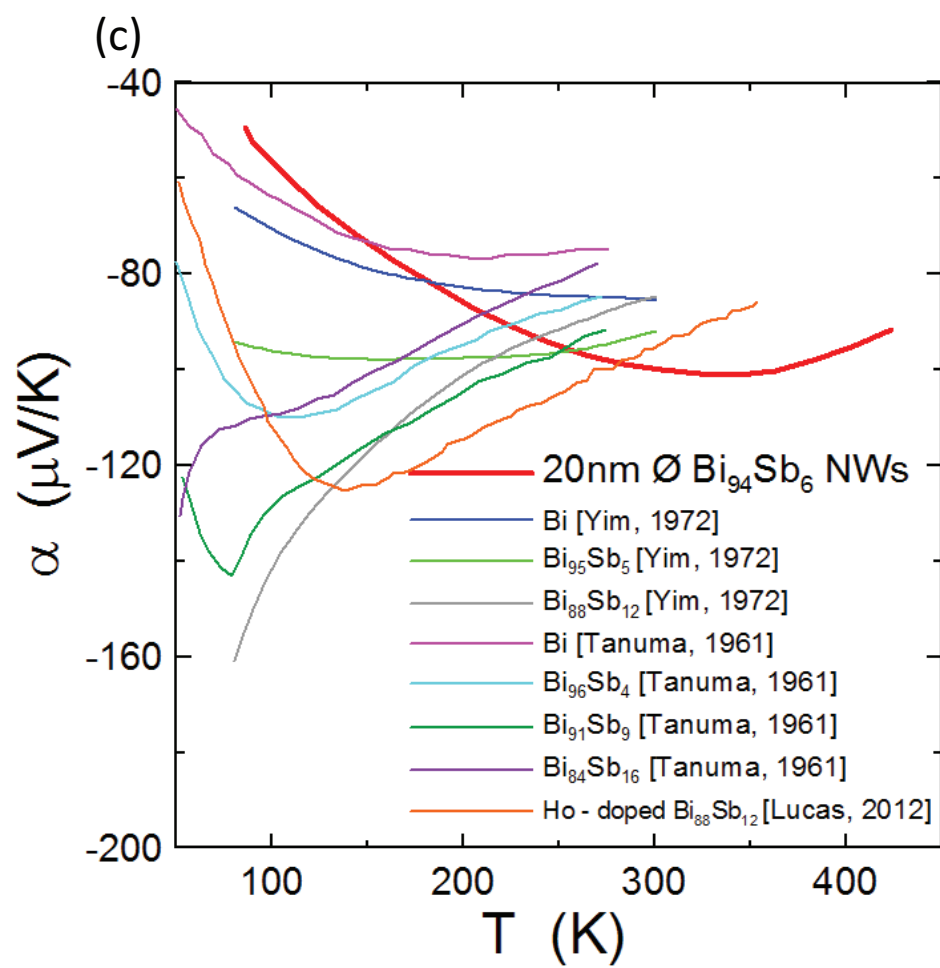


Fig. 8c

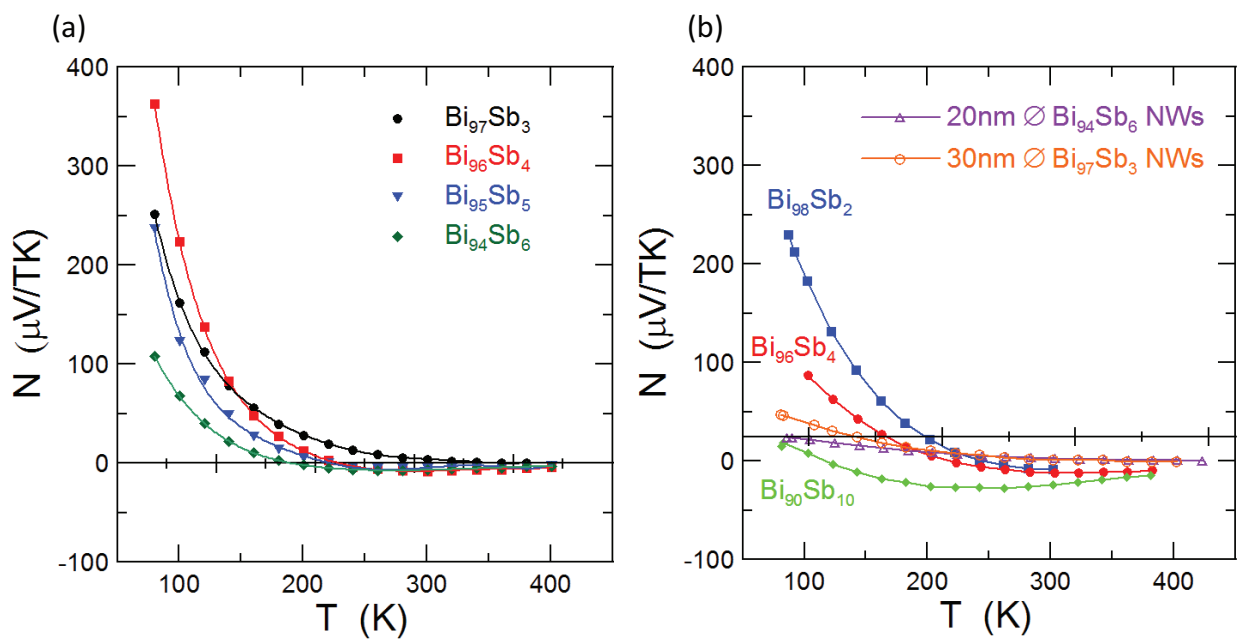


Fig. 9

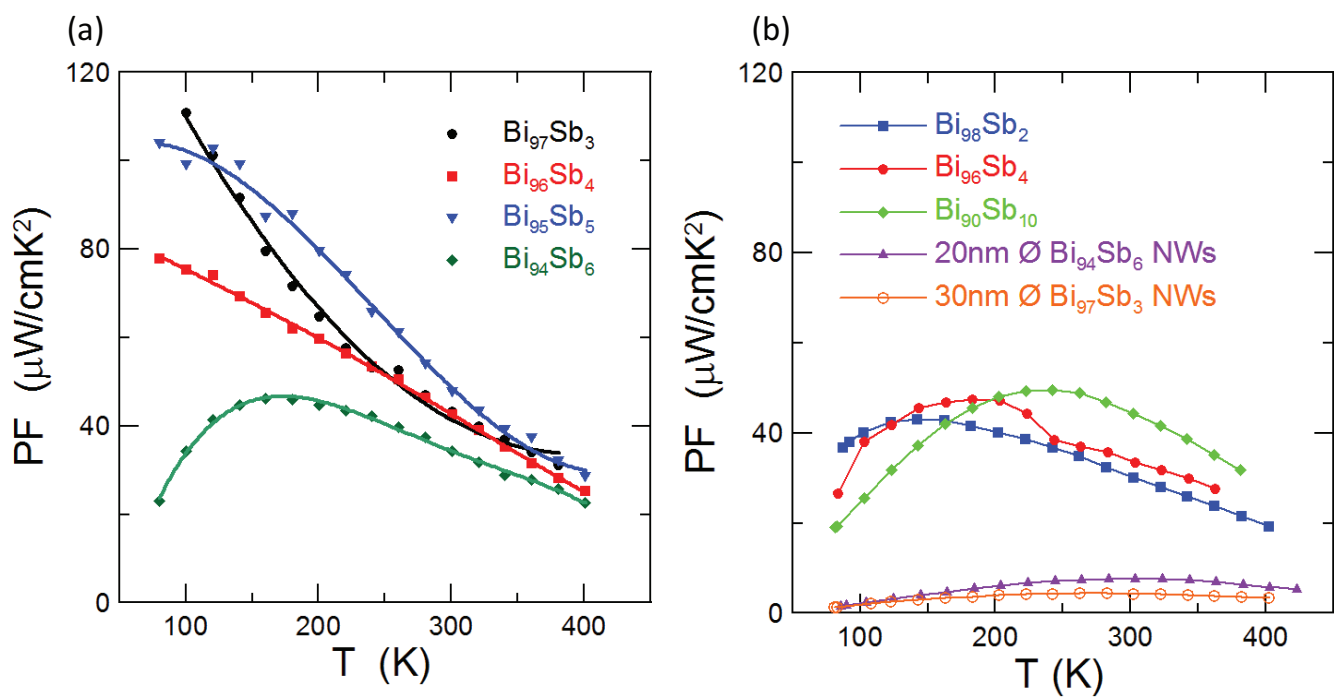


Fig. 10

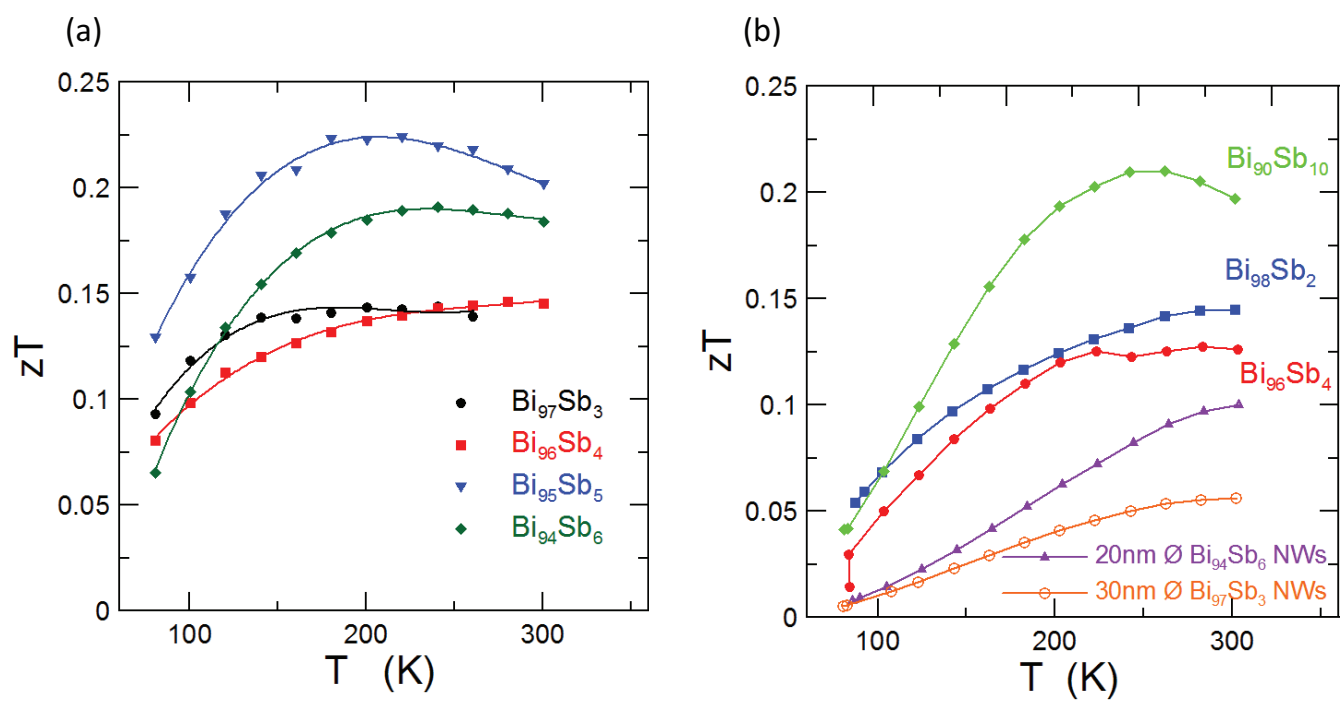


Fig. 11